npj computational materials

www.nature.com/npjcompumats

ARTICLE OPEN

Enabling rapid X-ray CT characterisation for additive manufacturing using CAD models and deep learning-based reconstruction

Amirkoushyar Ziabari[1]✉, S. V. Venkatakrishnan[1], Zackary Snow[1], Aleksander Lisovich[2], Michael Sprayberry[1], Paul Brackman[2], Curtis Frederick[2], Pradeep Bhattad[2], Sarah Graham[3], Philip Bingham[1], Ryan Dehoff[3], Alex Plotkowski[4] and Vincent Paquit[1]

Metal additive manufacturing (AM) offers flexibility and cost-effectiveness for printing complex parts but is limited to few alloys. Qualifying new alloys requires process parameter optimisation to produce consistent, high-quality components. High-resolution X-ray computed tomography (XCT) has not been effective for this task due to artifacts, slow scan speed, and costs. We propose a deep learning-based approach for rapid XCT acquisition and reconstruction of metal AM parts, leveraging computer-aided design models and physics-based simulations of nonlinear interactions between X-ray radiation and metals. This significantly reduces beam hardening and common XCT artifacts. We demonstrate high-throughput characterisation of over a hundred AlCe alloy components, quantifying improvements in characterisation time and quality compared to high-resolution microscopy and pycnometry. Our approach facilitates investigating the impact of process parameters and their geometry dependence in metal AM.

npj Computational Materials (2023)9:91 ; https://doi.org/10.1038/s41524-023-01032-5

INTRODUCTION

Characterisation is critical for understanding the processing, microstructure, and properties of materials and then correlating them with their performance. 3D X-ray computed tomography (XCT) is a commonly used characterisation process for non-destructive evaluation of additive manufacturing (AM) components[1–3], characterisation of batteries[4,5], components in automotive[6–9], casting[10,11], aerospace[12–14], and nuclear industries[15,16]. During an XCT process, the object under study is centered on a stage and then rotated around its vertical axis. At predetermined view angles during rotation, a 2D projection of the X-ray source passing through the part is captured by the detector. From the stack of 2D projection data, an algorithm is used to reconstruct a 3D attenuation coefficient map as a representation of the scanned object. An analytical algorithm, known as Feldkamp, Davis, and Kress (FDK)[17], is commonly used by commercial industrial XCT systems for 3D reconstruction.

In AM, the reconstructed 3D volumetric image from an XCT scan of the object is used to extract information about dimensional accuracy[18,19], defect distribution and density[20–24], and surface roughness[25–27] of the printed parts. XCT can also be beneficial in enhancing modeling and simulation capabilities to enable predictive design of materials and manufacturing processes[28,29]. Evaluating AM parts as soon as they are printed allows for tracking the changes after assembly that cannot easily be achieved with other characterisation methods[30–32].

Despite its prevalent use, XCT has several limitations that continue to degrade its performance when applied to metal AM components. For example, high-quality FDK reconstructions require long scan duration and complex post-processing image analysis, which has significant cost implications[33]. Reducing scan times, either by reducing the number of 2D projections acquired (sparse-view CT) or by reducing the integration time for each projection (low-dose CT), reduces FDK image quality and introduces severe artifacts. These issues further complicate the post-processing image analysis and defect detection tasks required for characterisation of the parts[32].

Another major challenge in metal additive manufacturing (AM) is the beam hardening (BH) effect for dense metal parts[34,35]. Conventional XCT algorithms implicitly assume a monochromatic X-ray source, but the polychromatic nature of the X-ray source causes this assumption to fail for thick, dense materials like metals. The resulting BH effect creates severe artifacts in reconstructed XCT images, particularly for metal AM parts due to their complex geometry and photon starvation from low exposure times. These artifacts complicate accurate image analysis and inference tasks such as pore and defect detection.

Some sophisticated algorithms, mainly developed for medical XCT imaging, can account for nonlinear effects, e.g., BH, but are not easily adapted for industrial XCT systems due to computational costs or applicability limitations. For example, model-based iterative reconstruction (MBIR) with statistical parameter estimation[36] is computationally expensive and requires high-quality preliminary segmentation that can be challenging for sparse and noisy measurements of dense metal parts with complex geometries. A recent statistical approach[37] does not require segmentation but only works for medical imaging of tissues where bone thickness is small compared to tissue. Metal artifact reduction[38–40] approaches are not suitable for objects that are comprised of only dense materials, and they only work when the metal part can be identified perfectly from a preliminary scan. Linearisation methods[41,42] solely depend on offline calibration, and deep learning-based methods require significant numbers of real measurement data sets for training, which may not be feasible for industrial XCT applications. Furthermore, Supervised deep learning (DL)[43–46] methods often require high-quality reference reconstructions, which requires aforementioned non-DL-based approaches to create training data. Recently, iterative DL-based approaches[47] have

[1]Energy and Electrification Infrastructure Division, Oak Ridge National Laboratory, Knoxville, TN 37830, USA. [2]ZEISS Industrial Metrology LLC, Maple Grove, MN 55369, USA. [3]Manufacturing Science Division, Oak Ridge National Laboratory, Oak Ridge, TN, USA. [4]Materials Science and Technology Division, Oak Ridge National Laboratory, Oak Ridge, TN, USA. ✉email: ziabariak@ornl.gov

been proposed to address BH, but they are computationally expensive and require substantial memory when processing large data sets in industrial XCT. Industry-standard solutions require an expert user to correct BH by manually selecting the coefficients of a polynomial filter after reconstruction[48].

In this work, we developed a supervised DL-based approach that leverages computer-aided design (CAD) models of the printed parts, as well as physics-based information for XCT reconstruction of metal AM parts to address these challenges. In this approach, we designed and trained a residual 2.5D[49] convolutional neural network (CNN) built on a modified U-Net architecture[50] to find a nonlinear mapping from a limited number of sparse FDK reconstructions of select reference parts to corresponding high-quality CAD-assisted MBIR[51,52] reconstructions of densely sampled scans of the same parts. The trained network, CAD-based Deep Learning MBIR (CAD-DLMBIR), produces fast (on par with analytical approaches) and accurate 3D volumetric reconstruction images of the parts, with reduced metal artifacts and BH, from their respective sparsely measured (i.e., with a low number of views) XCT scans. In a case study, we demonstrate that even when we reduced the number of views by a factor of three from 580 views to 193 views per coupon, we were able to obtain more accurate and higher quality characterisation (verified using multiple techniques) compared to the traditional algorithms. Further, in order to obtain the same quality of characterisation as ours using the traditional algorithm, we would require a factor of more than three denser scan[53–57] compared to the scan with 580 views, suggesting that our approach leads to an overall acceleration of high-quality characterisation by a factor of more than nine times.

The improved contrast and artifact reduction also resulted in notable improvements in post-processing analysis of the reconstruction data. We demonstrate that our method using sparse scans allows for detecting more than about 78% of flaws larger than 50 μm, and 100% of the flaws larger than 90 μm, while the corresponding numbers for the standard FDK X-ray CT reconstruction, for the same scan setting, is 18% (for larger than 50 μm) and about 70% (for larger than 90 μm), and can only detect 100% of pores that are larger than 170 μm.

The key contributions of this work are as follows:

1. ***Fast and accurate sparse-view XCT algorithm for metal parts***
   - A CAD and physics-based BH and metal artifact reduction method was developed (CAD-BHMBIR) to correct the raw, measured XCT projection data used in MBIR algorithms for high-quality reconstruction of parts.
   - A 2.5D residual network based on a modified U-Net was designed and trained to learn a nonlinear mapping between FDK reconstruction and CAD-BHMBIR reconstruction of pairs of data for training volumes (three parts in this study).
2. ***Extensive validation of XCT using proposed approach***
   - Independent pycnometry and optical microscopy measurements were used to evaluate and verify the enhanced defect detection capability offered by the proposed approach.
   - We demonstrate rapid and reproducible characterisation of parts using non-destructive XCT imaging, automated image analysis, and reporting to enable accurate analysis of porosity, pore size/shape distribution, and deformation mapping.
3. ***Enabling rapid and high-quality batch characterisation of more than a hundred metal parts, that can be leveraged in systematic studies in AM.***
   - Using this method we were able to experimentally shed light on geometry dependence of the impact of process parameters on the quality of the printed parts.

RESULTS AND DISCUSSIONS

DL framework for XCT reconstruction

An overview of the proposed framework is shown in Fig. 1, that consists of three main blocks. Figure 1a highlights the first block, CAD-BHMBIR (CAD-based Beam Hardening corrected MBIR), which uses the CAD model of the scanned parts along with physics-based information to produce a high-quality reconstruction of the part. Figure 1b shows our supervised DL approach, CAD-DLMBIR. In this second block, the network learns a nonlinear mapping from the low-quality analytical reconstruction (FDK), which suffers from artifacts and noise owing to the sparsity of the scans (fast scans with a limited number of projection views) as well as BH, to the high-quality iterative reconstructions generated by CAD-BHMBIR, which leverages the CAD models of the parts to reduce the noise and BH artifacts. The last block, shown in Fig. 1c, is the trained network under deployment during testing, where new sparse measurements are input to the trained CAD-DLMBIR network and the output will be the high-quality reconstruction approximating CAD-BHMBIR output. In the following sections, we provide more details about each of these blocks.

CAD-BHMBIR

MBIR[51,52] is a powerful approach for obtaining high-quality reconstructions in challenging scenarios, such as in low signal-to-noise ratio, limited-view, and sparse-view data sets across applications[58]. MBIR approaches cast the reconstruction as a minimisation of a cost function that has two sets of terms—one that enforces fidelity of the reconstruction to the measured data and the other that regularizes the solution to have some desirable properties. Specifically, we cast the reconstruction as

$$\hat{\mathbf{x}} \leftarrow \arg\min_{\mathbf{x}} \left\{ \frac{1}{2} \|\mathbf{y} - \mathbf{A}\mathbf{x}\|_{\mathbf{W}}^2 + r(\mathbf{x}) \right\} \tag{1}$$

where $\mathbf{y}$ is the measured CT data, $\mathbf{A}$ is a forward model describing the cone-beam CT geometry, $\mathbf{W}$ is a diagonal noise covariance matrix set so that $W_{ii} = \lambda_i$, λ_i is the dark-field corrected raw count data, and $r(\mathbf{x})$ is a regularizer based on the q-generalised Gaussian Markov random field model[59].

While in the past, and mainly in the context of medical XCT imaging, MBIR techniques have been used to address BH[36,37], they cannot be readily applied to industrial XCT of metal AM parts because the techniques require a perfect à priori segmentation of the parts, as well as a significant computational burden for estimating the BH correction factors.

In contrast to existing approaches, in this study, we leveraged the CAD model of the part to be scanned to estimate an accurate filter to correct for BH. Furthermore, we assumed that the source spectrum and detector characteristics are not known. Once the correction BH filter was obtained, we filtered the projection data and used it in MBIR to produce a high-quality reconstruction of the parts. Figure 2a summarizes the BH removal process. We began by simulating the projection data of XCT measurement corresponding to the CAD model of the object. We used the phenomenological bimodal energy model proposed by Van de Casteele et al.[41] to accurately approximate the beam propagation using two dominant energies in the X-ray source beam. Assuming E_1 and E_2 as the two dominant energies of the source, one can write

$$-\log\left(\frac{I}{I_0}\right) = \mu(E_2)d + \log\left(\frac{1+\alpha}{1+\alpha e^{-(\mu(E_1)-\mu(E_2))d}}\right) \tag{2}$$

where I is the attenuated intensity, I_0 is the reference bright image intensity (a projection with no object in between), and d is the thickness. $\mu(E_1)$, $\mu(E_2)$, and α are the model BH parameters and can be obtained by fitting a simulation of the CAD model to the experiment. We ran simulations with a CAD model and compute $\mu(E_1)$, $\mu(E_2)$, and α to fit a slice from the reconstruction output to a

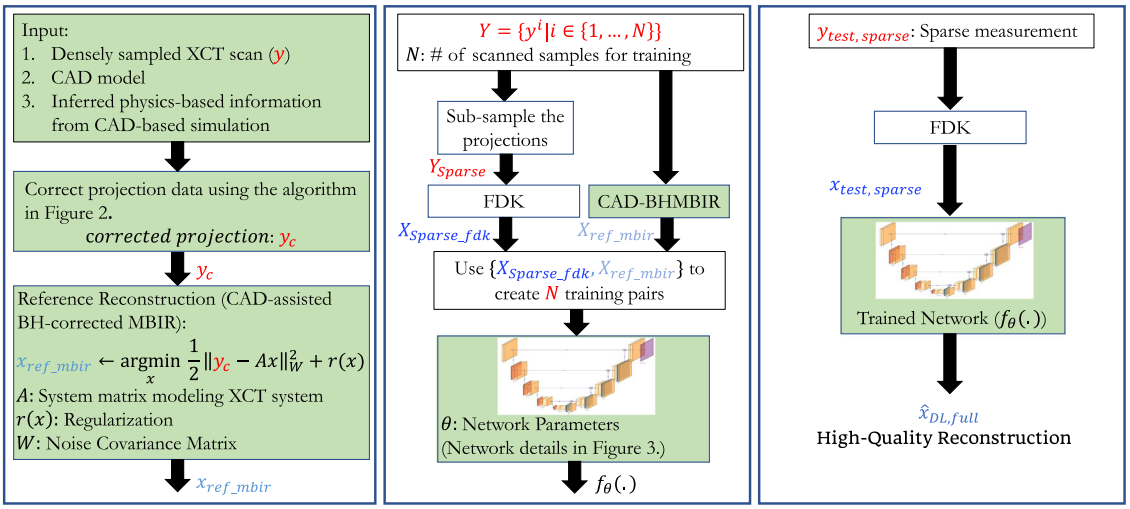

Fig. 1 Overview of the proposed approach, which consists of three blocks. a The first block allows us to produce high-quality reference reconstructions via CAD-BHMBIR (details provided in Fig. 2). **b** In the second block, we train the network on multiple pairs of training data, where the input is the inferior quality FDK reconstruction from sparse scans and the target is the corresponding CAD-BHMBIR reconstruction of densely sampled scans (details of architecture provided in Fig. 3). **c** The third block shows how the network is being deployed to produce high-quality reconstruction on new sparsely measured data. The novelties and contribution of this work are highlighted in green.

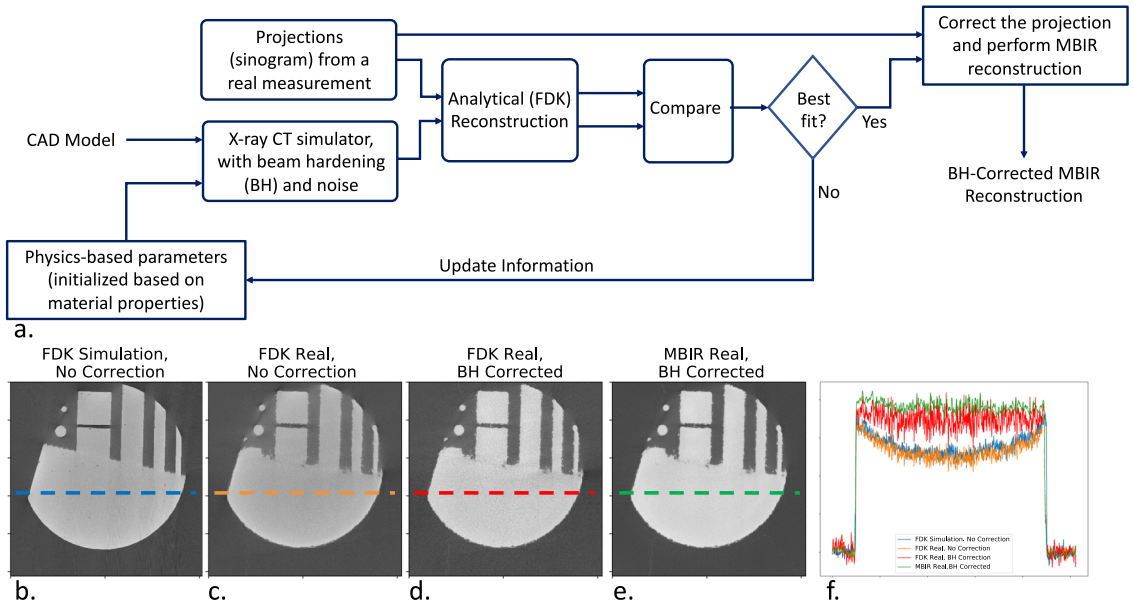

Fig. 2 Procedure to suppress BH using CAD model and physics-based simulation and example results. a The diagram shows that optimum BH parameters are calculated and updated until simulation fits real measurement. Then knowing the parameters, we can correct the measured projections (see the text) and perform the final reconstruction. A slice from, (**b**) FDK reconstruction of the CAD-based simulated part with BH and noise. This simulation is done with the final fitting parameters; (**c**) FDK reconstruction of a real data set with no correction applied for BH; (**d**) FDK reconstruction of a real data set after BH correction; (**e**) MBIR reconstruction of a real data set after BH correction; (**f**) Line profile comparison between slices shown in panels (**b**-**e**) along the vertical dashed line.

corresponding slice from the real data set[35]. As shown in Fig. 2a, we iteratively adjusted the parameters so that the final reconstruction obtained from the simulated data had a similar profile to the experimental data.

Once we optimised the BH model, so that the reconstruction from the CAD model–based simulated data matched the experimental data, we used the coefficients of an eighth order polynomial to correct the simulated data and suppress BH artifacts in the reconstructions from the simulated projection. We then used this learned filter to correct the projection data obtained from the experimental XCT scans, which were passed to MBIR for final high-quality reconstruction. An example slice from the 3D volume of the simulated data is shown in Fig. 2b. The data were registered and compared with a corresponding slice from a real measured XCT (as shown in Fig. 2c) with a standard reconstruction algorithm (FDK). Even though the measurement settings were set to run the scan in a reasonable amount of time while producing good contrast and noise properties by industrial standards, the

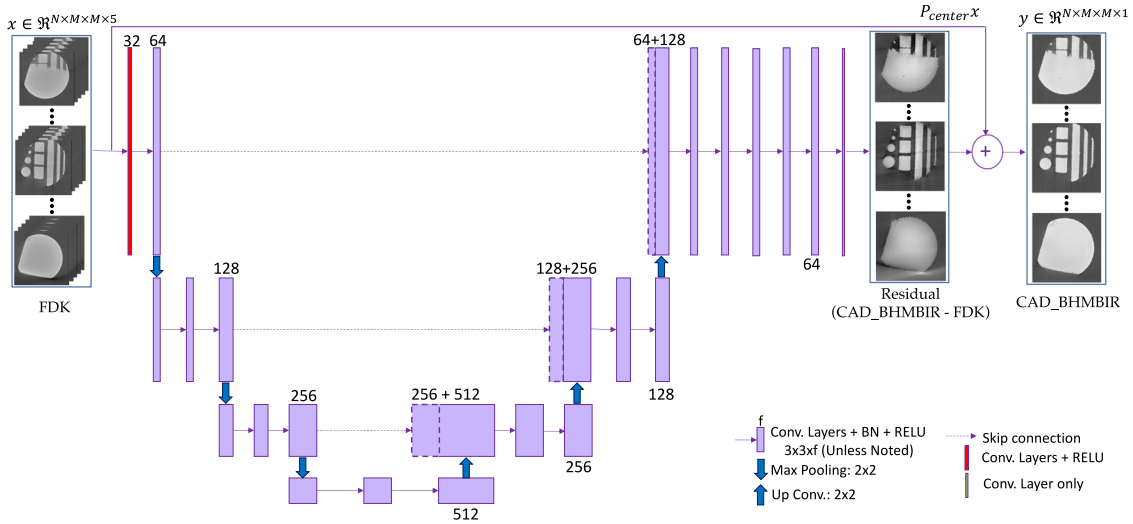

Fig. 3 2.5D CAD-DLMBIR architecture based on a modified U-Net architecture. Network trained on pairs of N patches of $M \times M \times 5$ FDK slices and $M \times M \times 1$ slices from the CAD-BHMBIR. These patches are created from 3D volumes. Compared with the original U-Net architecture, the modified U-Net architecture uses batch normalisation in the middle layers, and three convolutional layers are added at the end. The softmax function at the end layer is also dropped because the network is trained for residual between ground truth and FDK input.

typical FDK reconstructionwas limited by BH, scattering, and noise. The corresponding CAD-assisted, BH-corrected reconstructions using FDK and MBIR are shown in Fig. 2d, e. A comparison for profile lines along the slices is shown in Fig. 2f. The cupping effect at the center (brighter edges and darker interior) is clearer in the profile corresponding to Fig. 2b, c (blue and orange profile lines), which is removed in the profiles corresponding to Fig. 2d, e (green and red profile lines). The FDK reconstruction with the corrected projection data resulted in a BH-corrected but noisy image volume. The lower noise and better quality of a profile (green line in Fig. 2f) across an MBIR slice in panel (e) are also evident.

2.5D CAD-DLMBIR

Although it produces high-quality reconstructions, performing CAD-BHMBIR for characterisation of hundreds of parts is computationally prohibitive and would take several weeks to complete for typical high resolution XCT scans even when using an eight GPU-based system described in methods (sub-section i). Instead, we used CAD-BHMBIR to produce reference high-quality reconstructions for training our DL-based approach. As shown in Fig. 1b, the main goal of the DL-based approach is to suppress the significant noise and BH artifacts from low-quality analytical (FDK) reconstructions of the sparse data to produce a high-quality reconstruction approximating CAD-BHMBIR reconstruction of densely sampled data while being able to run in near real time due to the low computational complexity. To achieve this goal, we trained our network on pairs of FDK reconstruction of sub-sampled scans (FDK-Sparse) to CAD-BHMBIR of densely sampled scans. The architecture for the deep learning convolutional neural network is shown in Fig. 3, which was designed based on a modified U-Net architecture[50]. Details of training, testing, as well as training and test data sets and parts are provided in methods (sub-sections a-d).

For the sake of comparison and evaluation of our approach, we also trained a second network between pairs of FDK and CAD-BHMBIR reconstructions of densely sampled data. This network was used to create high-quality reference data for each individual test part and to evaluate the performance of the proposed approach. To summarise, the two trained networks are as follows:

1. **CAD-DLMBIR-Sparse**: trained on pairs of FDK of sub-sampled scans (FDK-Sparse) to CAD-BHMBIR of densely sampled scans
2. **CAD-DLMBIR-Dense**: trained on pairs of FDK of densely sampled scans (FDK-Dense) to CAD-BHMBIR of the same scans (only for creating reference and avoiding the need to perform long iterative reconstruction for every test part)

Printed test parts

The geometry of the test specimen is shown in the inset of Fig. 4d, where we color-coded and identified individual geometric features. It contains a cylinder with approximately 15 mm diameter and a flat surface to simplify the registration between measured data and the CAD model. Furthermore, on top of the cylinder, three distinct geometries were printed: walls (fins) of different widths, inclined bars at different angles, and small rods of different diameters. Overall, the full geometry fits approximately in a $15 \times 15 \times 15\,mm^3$ full cylinder. The special design of this specimen serves three purposes. First, the thick cylinder portion is to cause significant beam hardening. Second, the top geometric features allow for creating complex XCT reconstruction artifacts. And third, this design aids in investigating the impact of geometry on optimising the printing process parameters for a new material. Specifically, the solidification and cooling rates during print for these features are expected to be different than the bulk part, and, in turn, their porosity levels should be different as a function of printing process parameters. We printed 123 test specimens on two build plates using various process conditions and parameters of interest using an LPBF system. Details of process parameters are provided in SI.

Case studies

Here, we present case studies highlighting the importance of the proposed approach. The main goal of the case studies is to show that the proposed approach considerably reduces scan time while producing high-quality results with reduced noise and BH artifacts. We also show that the high-quality reconstruction enables superior defect detection and more consistent characterisation capabilities, which are critical for confirmation of this tool for certification and qualification of metal AM parts.

First, to determine the efficacy of the CAD-DLMBIR technique, we compared the XCT reconstructions of a part with a corresponding high-resolution micrograph obtained through optical microscopy. To that end, a test part was XCT scanned

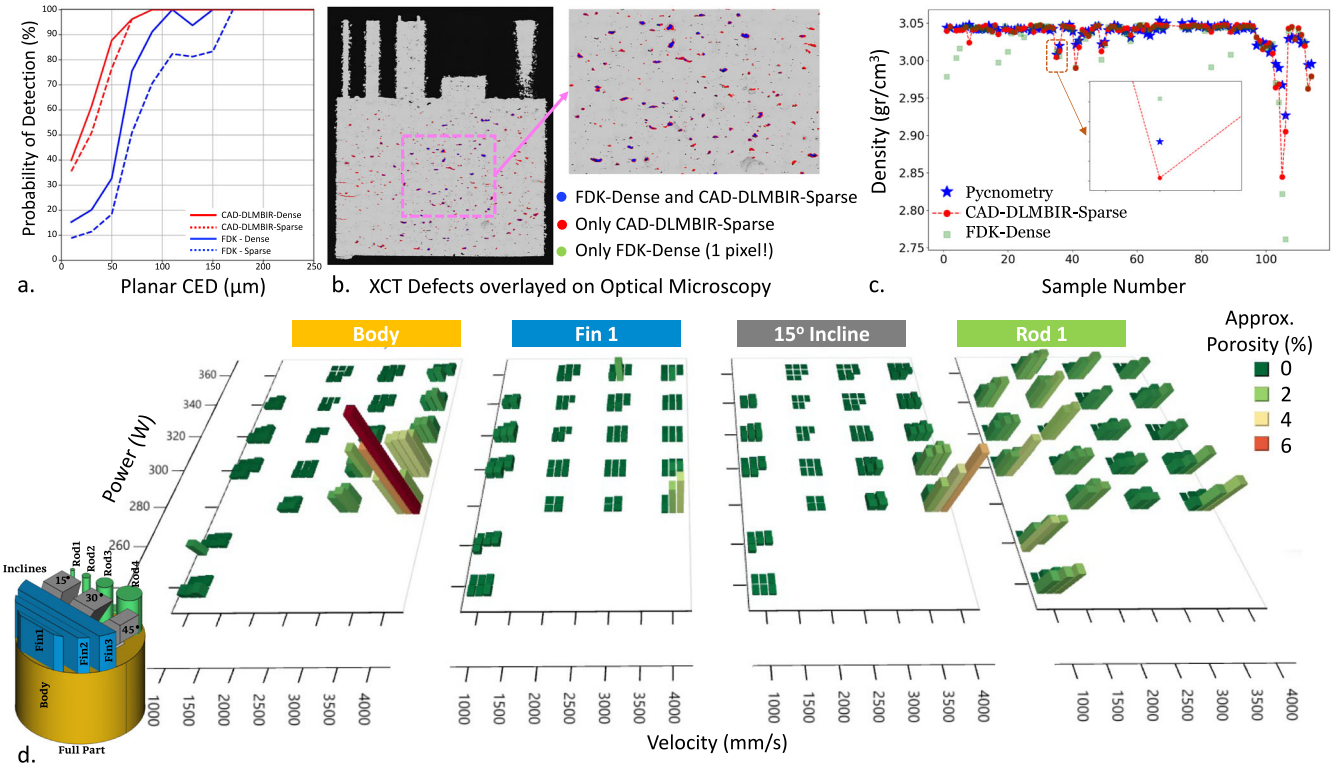

Fig. 4 Comparison of the flaws successfully detected by the FDK and CAD-DLMBIR reconstructions. a Probability of Detection (PoD) curves[74] (see methods, subsection **b**) for the four XCT reconstructions using different algorithms for one of the parts (identified in the inset of the panel (**c**)); and (**b**) an overlay of the successfully detected flaws in both the FDK-Dense and CAD-DLMBIR-Sparse reconstructions. **c** Density comparison with pycnometry for 123 parts printed with different printing process parameters. The proposed approach shows 43% improvement in RMSE, while using a sparse scan with 193 views. Segmentation for each FDK-Dense reconstruction may be individually tuned and improved, but it will take a significant amount of time and effort. On the other hand, the consistency of reconstructions by CAD-DLMBIR-Sparse simplifies the automation and high-throughput analysis of scanned parts. The inset in panel (**c**) corresponds to density values for the part used in panels (**a**) and (**b**). **d** Analysis of porosity in different geometric features of the printed parts (features are named on the geometry on the bottom left). Multiple sets of optimal printing parameters in the same build as a function of geometry were observed. The segmentation (flaw detection in X-ray CT) was performed using algorithm described in methods subsection **d**.

and then cut and prepared for optical microscopy to capture its polished surface. A semi-automatic registration approach was used to register the 2D micrograph to 3D XCT volumes. Details of the registration approach and some comparisons between reconstructions are provided in the methods (sub-section f) and the Supplementary Fig. 5, respectively.

Close inspection of the reconstructions indicates that CAD-DLMBIR facilitated the detection of smaller flaws compared with traditional FDK reconstruction. This is shown quantitatively in the probability-of-detection (PoD) curves in Fig. 4a, where we plotted the probability density function–like (pseudo-PDF) representations of the PoD curves for the four XCT reconstructions (see sub-section b in methods for calculation of PoD values and graphs).

Figure 4 shows that the CAD-DLMBIR reconstructions significantly outperformed the standard FDK reconstructions in terms of their ability to detect flaws—despite the application of an identical flaw detection algorithm tuned to favor FDK. For example, the FDK-Sparse reconstruction was only able to successfully detect approximately 80% of flaws with circular equivalent diameters 100 μm (about 6 pixels at a voxel size of 17.3 μm used in these scans noted in methods) or larger. Increasing the number of views resulted in a 96% detect rate for flaws 100 μm or larger, whereas both CAD-DLMBIR reconstructions, regardless of their number of views, were successfully able to detect all flaws with circular equivalent diameters (CEDs) 100 μm or larger. Below flaw sizes of 100 μm, flaw detectability in the two FDK reconstructions dropped precipitously. The FDK-Dense reconstruction only achieved PoDs of 20% for flaws larger than 25 μm, and 32% for flaws larger than 50 μm. The FDK-Sparse reconstruction only achieved PoDs of 12% for flaws larger than 25 μm, and 18% for flaws larger than 50 μm. In contrast, the CAD-DLMBIR-Sparse reconstruction was successfully able to detect 50% of flaws larger than 25 μm (slightly larger than 1 pixel), 78% of flaws larger than 50 μm (about 3 pixels), and 100% of the flaws larger than 90 μm (about 5 pixels). Thus, even with a sparse scan with only 193 views, the CAD-DLMBIR volume demonstrated a marked 2.5–4.3 × improvement in flaw detectability compared with the FDK-Dense and FDK-Sparse reconstructions, with 580 and 193 views, respectively. The superior detection capability furnished by CAD-DLMBIR-Sparse reconstruction is shown qualitatively in Fig. 4b, which compares the flaws that were successfully detected by the FDK-Dense and CAD-DLMBIR-Sparse volumes.

Next, we compare the 3D XCT reconstruction results from different algorithms. Figure 5 depicts three slices from X-Y, X-Z, and Y-Z views of the 3D volume, reconstructed using the four aforementioned algorithms. As noted, we trained a second network, CAD-DLMBIR-Dense, that serves as the reference data to avoid the necessity of performing a computationally expensive iterative reconstruction for every part. FDK-Dense is the output of the standard reconstruction algorithm being used, and FDK-Sparse is the standard reconstruction output when reducing the number of views by a factor of 3. More figures and volumes are provided in the Supplementary Figs. 2–4.

The figures demonstrate that the CAD-DLMBIR-Sparse produced high-quality reconstructions (comparable to CAD-DLMBIR-Dense) and showed significant improvement compared with the standard

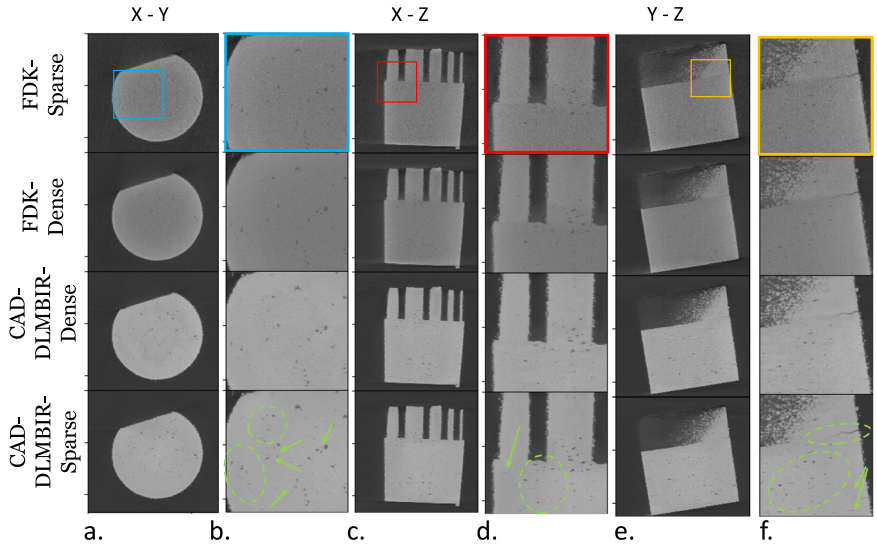

Fig. 5 Qualitative cross section comparisons across different views. FDK and CAD-DLMBIR reconstructions are shown both for Sparse and Dense scans. (**a**) X-Y slice and (**b**) expanded view of highlighted region in (**a**). **c** X-Z slice and (**d**) expanded view of highlighted region in (**c**). **e** Y-X slice and (**f**) expanded view of highlighted region in (**e**). Noise was significantly reduced and several of the pores/defects that were less clear in FDK-Dense data and completely smeared in FDK-Sparse data were restored in CAD-DLMBIR results with high contrast (in both CAD-DLMBIR-Dense and CAD-DLMBIR-Sparse). Some examples are marked with an arrow (smaller flaws) and are highlighted inside a circle.

reconstruction algorithms. These results are highlighted with arrows and dashed circles in the figure panels. These figures shows that despite reducing scan time by a factor of three, the proposed approach can maintain the quality of the reconstruction.

To further quantify the improvements observed, we segmented the flaws (e.g., defects, cracks, pores) in different reconstructions for all parts in the set. The segmentation (flaw detection in X-ray CT) was performed using the algorithm described in methods (sub-section d). From those segmentation results, we calculated the density of flaws in the parts and compared the results with pycnometry. Helium pycnometry[60] is a standard method for density measurement of AM parts (see details in methods). The main drawback of pycnometry is that it is a point measurement and cannot provide any details regarding the spatial or morphological distribution of part defects. To obtain the density of the volumes (Δ) from segmentation of flaws in reconstruction, we used $\Delta = 100^*(1 - V_p/V)$, where V_p is total computed volume after segmenting out the pores/defects, and V is the volume with all the flaws filled. We normalised density values based on the median of the pycnometry data. The results are shown in Fig. 4c. The root-mean-squared-error (RMSE) between density extracted by CAD-DLMBIR-Sparse and pycnometry is 0.01445, and for FDK-Dense and pycnometry is 0.0255, which is about 43% improvement across all the parts. The inset in Fig. 4c shows the density for the part used in Fig. 4a, b, which shows a seemingly small change in the extracted density could be correspond to a large detection capability between the two reconstructions. Note that pycnometry measurements are mostly affected by the presence of large internal voids, such as lack-of-fusion, due to the cubic scaling of volume with flaw size. Therefore, even a small difference in measured density can correspond to a large effect on detection capability due to the rapid degradation of the PoD for smaller flaw sizes. Although the results (both pycnometry and PoD calculation) suggest a significant improvement in porosity analysis and flaw detection using CAD-DLMBIR-Sparse compared with FDK-Dense and FDK-Sparse, this is not the sole goal since segmentation for each FDK reconstruction may be individually tuned and improved. This individual process will, however, take a significant amount of time and effort, which adds to the already complex and time-demanding task of printing process parameter optimisation. Conversely, the consistency of reconstructions by CAD-DLMBIR (both Sparse and Dense scans) simplifies the automation and high-throughput analysis of scanned parts.

Fast and high throughput characterisation

In addition to generating high-quality 3D reconstruction volumes with reduced noise and artifacts, the proposed approach allows for fast and consistent reconstructions, which simplifies the automation of fast characterisation and parameter optimisation process of AM parts. Such high-quality, fast and consistent reconstruction enables accurate quantification of flaw sizes and morphology, and study their effects on the mechanical performance and properties of the printed part. This is a major step toward qualification and certification of AM parts that has historically been a bottleneck preventing AM from reaching its full potential[61].

Previous work has demonstrated development of the Al-Cu-Ce(-ZR) family of alloys which produce a desirable combination of mechanical properties and printability[62,63]. Here, to illustrate the impact of our method, we use CAD-DLMBIR to optimize process parameters for a new alloy, Al-9Cu-6Ce-1.85Zr, in this family. In Fig. 4d, we plot the porosity values for two printing parameters, velocity and laser power, for four of the geometrical features in all 123 printed parts. The figure emphasizes the importance of 3D geometry in selecting the optimal process parameters by comparing the porosity values for the cylindrical body of the part to the porosity in the smallest rod, smallest fin, and 15° inclines printed on top. The results indicate that the optimal process parameters can differ depending on the geometry even within the same part. More importantly, Fig. 4d highlights that the approach developed in this work enables analysis and high-quality characterisation of these small features in a larger metallic component, while performing batch non-destructive 3D X-ray CT scanning with sparse number of views in each scan. This approach provides extensive access to studying the 3D geometry dependence of process parameters in metal AM. Further comparisons and correlative studies can be made between porosity levels in different geometric features and various process parameters (refer to Supplementary Figs. 7–9 and corresponding text in supplementary note 5 for some examples).

One can achieve the same reconstruction quality by using iterative reconstruction on each measurement or performing a

new, very dense view scan and using FDK. The latter is a tedious task and would require significant testing and new measurements to achieve the same quality as the iterative reconstruction with fewer views. In fact, one popular choice for number of views to be used for a CT scan, under the assumption of a high signal-to-noise ratio (SNR), is setting the value to be equal to the number of detector columns[53] - which is 1840 in our case. Thus, to achieve an accurate reconstruction using the FDK algorithm, one needs to perform scans with at least a factor of three ($1840/580 \approx 3.1$) more views than what we have used in our "dense scan" experiments. This in turn results in an overall scan time which is at least 9.3 times more than our experiments using sparse-view data combined with CAD-DLMBIR.

The alternate approach of using a sparse view scan, like in our studies, combined with fully iterative reconstructions, is also not trivial and would require prohibitive amount of computation for fast reconstructions using currently available open-source implementations. Iterative approaches in the literature[64–66] take at least several hours to complete one volume (at least 6 hours per volume for the data in this work) using an eight GPU computing resource as noted in subsection e in methods. These scenarios are time-consuming, making high-throughput batch characterisation cumbersome. Our proposed approach significantly shortens the total characterisation time for the 123 coupons, which would take more than 10 days using the standard approach with FDK ($2h \times 123$). Using our approach, the total time is about 1.2 days for 123 scans and 123 reconstructions using CAD-DLMBIR. One day dedicated to model training increases the total time for the first run to 2.2 days. Note that the training step can be performed offline. Also, every new scan will only take about 14 min total for scan and reconstruction.

An interesting observation in the results is the fact that the training was done on three parts with maximum 0.14% porosity, about 3300 flaws and 0.0007 mm^3 average pore size. During testing, however, the network produced consistent and accurate results for parts as porous as 6.7% with more than 22,000 flaws and 0.006 mm^3 average pore size. It is worth noting that the part used in Fig. 4a is 1.5% porous with about 16,000 pores and average pore size of 0.0018 mm^3, which are all well-above what the network was trained on. In addition, while the network training is offline and can be trained for different materials, we tested the model's generalisability by applying the same trained network in the shown case studies to other alloys. To that end, we tested the network on parts printed using AlSi, Inconel, and 316 steel alloys. In the case of similar alloys or alloys that are measured with the same measurement setting (even with a different geometry than what we trained on), we only need to ensure that the median of the intensity values of two modes available in the images (material and background/air) matches between training parts and the inference parts. Therefore, before inference, we apply a pre-processing step that performs a simple Otsu threshold[67] on the input images, clusters them to two groups, and linearly matches the median of the input to median of the clusters recorded during training. The inverse of this linear operation will be applied to the output to return actual intensities. An example demonstrating the generalisability of the approach is shown in Supplementary Figure 11. We emphasise that these are only preliminary results and a thorough investigation of generalisability of the approach is a subject of our future studies.

In summary, this study demonstrates a powerful approach for characterisation of metal AM that can be applied to produce consistent characterisation of AM parts and be used to find optimal printing process parameters for novel alloys in LPBF. We quantified the significant improvement in scan quality and scan acquisition time using high-resolution optical microscopy images as references. Comparison with pycnometry demonstrated remarkable agreement that (to the best of our knowledge) has not been achieved in previous reports comparing XCT and pycnometry. Such improvement will lower the cost of characterisation (for both labor and maintenance) and provide consistency for qualification and certification of AM parts, which is currently preventing AM from reaching its full potential. The method allowed us to investigate regions of optimum process parameters and their geometry dependence for LPBF printing of Al-9Cu-6Ce-1.85Zr alloy from Al-Cu-Ce(-ZR) family of alloys. The proposed approach paves the way for automating the inline characterisation of AM parts and providing seamless feedback to the printing systems.

METHODS

Training

The DL architecture for our network is shown in Fig. 3, which was designed based on a modified U-Net architecture[50] to perform residual learning to suppress artifacts and noise. Compared with the original architecture[50], the last softmax layer was omitted since we did not perform classification. Rather, we needed full size images, so three additional convolution layers (Conv2D, Relu, and BatchNorm) were added before the final 1×1 convolution. Batch normalisation was also added in the intermediate layers to stabilize the network and to provide better convergence. More importantly, and inspired by our prior work[68], we trained the network in a 2.5D manner. 2D networks learn a nonlinear mapping between pairs of 2D input/target images (all the convolutions are in 2D), while 3D networks learn a nonlinear mapping between pairs of 3D input/target images (all the convolutions are in 3D). Unlike 2D and 3D networks, 2.5D networks learn a mapping between a 3D input and 2D output. A sliding window strategy was employed to create 3D patches of training data. The patch size in our work was 256×256 in the in-plane direction (X-Y), and 5 in the cross-plane (Z) direction. The stride for the patches size was 128 in the X-Y direction and 1 in the Z direction. Therefore, each training pair included a $n \times n \times 5$ FDK input and $n \times n \times 1$ MBIR target, where n is 256. The network absorbed the 3D information by taking 5 neighboring slices as input, and from each 5 neighboring slices, it learned the mapping to the center target slice. The number of neighboring slices was chosen based on the analysis by Ziabari et al.[68]. This approach allows for the 2.5D network to be nearly as accurate as a fully 3D network with significantly reduced computational cost (all the convolutions are in 2D). In fact, the 2.5D network is approximately the same inference speed as a 2D network and approximately the same quality as a 3D network.

The network minimizes a mean squared error (MSE) residual loss function

$$\ell(\boldsymbol{\theta}) = \frac{1}{2N}\sum_{i=1}^{N}\left(R(\boldsymbol{x}_i;\boldsymbol{\theta}) - (\mathcal{P}_{\text{center}}\boldsymbol{x}_i - \boldsymbol{y}_i)\right)^2. \tag{3}$$

Here, $\boldsymbol{x} \in \mathbb{R}^{N\times M\times M\times 5}$ and $\boldsymbol{y} \in \mathbb{R}^{N\times M\times M}$ are N batches of input and target training patches. A batch size of 32 was used during training of our neural network. Each batch of $\boldsymbol{x}_i$ contains 5 neighboring slices as input to incorporate the 3D spatial information, and $\boldsymbol{y}$ corresponds to the ground truth for the center slice of these neighboring slices. $R(\boldsymbol{x};\boldsymbol{\theta})$ is the nonlinear mapping learned by the network with $\boldsymbol{\theta}$ as network parameters. It takes batches of 5 neighboring slices and outputs the center residual slice estimated by the network. $\mathcal{P}_{\text{center}}$ is an operator projecting input $\boldsymbol{x}$ from 5 neighboring slices to the center slice in the batch i, which corresponds to the residual between the center slice of input and the target ground truth image.

We used 256,000 patches of data using a 80/20 cross-validation approach[69] for training. The 256,000 patches are created by extracting patches from the original data and performing 7 data augmentations. Since the original training volumes of data are of sizes $1000 \times 1000 \times 1000$, we crop them to individual patches of $256 \times 256 \times 5$ with a in-plane stride of 128 and cross-plane stride

of 3, that increases the number of training data. The 7 augmentations include in-plane, cross-plane, up-to-down, and left-to-right flips, rotations at 90, 180, and 270 degrees, and combinations of flips and rotations of the image patches. The augmentation of the validation set was separated from training set, so no common data were included in validation and training sets. To minimize the mean squared error residual loss function, we used the Adam optimiser[70] with an initial learning rate of 0.001 and default momentum setting. If the validation loss stagnated for 15 consecutive epochs, we reduced the learning rate by $2\times$.

Compared with the architecture discussed by Ziabari et al.[68], the new U-Net architecture learns local features better and renders more consistent results. An example comparison is provided in the Supplementary Fig. 1.

Testing

The last part of this framework is deployment for test parts, as shown in Fig. 1c. During testing, sparsely measured data is input to the framework and first reconstructed by the FDK. The FDK reconstruction is then input to the trained network to suppress noise and BH, producing a high-quality reconstruction.

Training data sets

To prepare training data, we scanned 3 parts produced by a metal AM printer. The level of porosity in the three parts used for training were 0.081%, 0.14%, and 0.12% with 1300 to 3,300 pores in the volume and an average pore volume between 0.0001 and 0.0007 mm^3. The standard setting recommended by the XCT system expert operator is set to 580 views at approximately every 0.35° with 1 s integration time and 4 image averaging per view angle. One scan takes nearly 39 min. It is worth noting that expert operators typically determine the setting empirically while considering trade-offs between quality of scans, cost and labour. The detector comprised 1456×1840 (rows × columns) with a pixel size of $0.127\times0.127\,mm^2$. CAD-BHMBIR was used to produce high-quality reconstructions that acted as target ground truths for training the DL network. Furthermore, as suggested in Fig. 1b, we produced input for training pairs of the DL network by sub-sampling the reference XCT raw projection data by a factor of 3, i.e., every 3 projections from 580 views in the scans were used to imitate an accelerated scan that acquired sparse data in a third of the default scan time (i.e., 193 views or almost 13 min). The sub-sampled sparse data were reconstructed using the FDK algorithm, which generated a reconstruction with significant BH artifacts as well as streak artifacts and noise due to the under-sampling. The three pairs of FDK reconstructions from the sub-sampled data and CAD-BHMBIR reconstructions from the densely sampled data served as a training set for CAD-DLMBIR. Unlike in the case of real-world natural images used to train deep neural networks, we have extremely limited training data comprising three volumetric reconstructions that have a size of approximately $1000\times1000\times1000$ voxels.

X-ray CT scanning

All the XCT scans were collected by ZEISS's Metrotom CT scanner. A shortscan[49,71] was used where only projections were acquired over a $[0, 180+2\alpha]$ range of projection angles. α is the cone beam fan angle. For these scans, the fan angle was $\approx 16°$, the tube voltage was set at 180 kV, and the current was set at 113 μA. In total, 580 projections were acquired for reference scans, and a third of those (i.e., 193 views) were for sparse scans. The specification for the flat panel detector used in the system can be found here: https://www.vareximaging.com/wp-content/uploads/2022/03/2520DX-I-Industrialpds.pdf. A 0.25 mm copper filter was used to reduce BH, and the voxel size in the scan was 17.3 μm.

Micrograph registration to X-ray CT and PoD

Post-build microscopy data were registered to the XCT data by applying differential evolution[72] to optimise a geometric transformation matrix mapping the micrograph to the XCT volumes. Additional details of the microscopy registration process are provided in the Supplementary Note 3. Once the micrograph was registered, flaws were identified in both the micrograph using thresholding algorithms, and compared against the flaws detected in the X-ray CT volumes using the segmentation approach described in methods subsection d. Flaws in the optical micrograph that were successfully detected by each XCT reconstruction were identified using the matching algorithm described by Sundar et al.[73]. The XCT PoD curves were generated by binning the flaws detected in the optical micrograph according to their circular equivalent diameter[74]. For each XCT reconstruction, the number of successfully detected micrograph flaws in each size bin were determined, and the PoD curves were generated by dividing the number of successfully detected flaws in the XCT data by the total number of optical micrograph flaws in that size bin. The PDF PoD curves can be interpreted as the probability of detecting flaws of a given flaw size, whereas the CDF PoD curves can be interpreted as the probability of detecting flaws of a given flaw size or above.

Pycnometry

In this work, helium pycnometry[60] served as ground truth for computing the overall density of the part to evaluate the density obtained by measuring the segmented pores from the reconstructed volumes. We used the Micromeritics AccuPyc II 1340 to perform pycnometry and measure skeletal density, which is the ratio of the mass of a solid material to the sum of the volumes of the solid and blind pores within the material (e.g., powders) (ASTM D3766). Using helium gas displacement as the mode, the system used the volume–pressure relationship of Boyle's law to calculate density. This process is relatively simple, but the greatest challenges to rapid turnaround are manual testing setup and data collection (despite access to new technologies).

Segmentation

The defect segmentation algorithm uses the image pre-filtering described by Sato et al.[75], which is based on computing the image Hessian and then applying the shape and size specific filtering selectively amplifying 3D objects of certain morphology, including elliptic shapes (i.e., pores), thread-like shapes (i.e., channels), and plates (i.e., cracks), followed by multilevel adaptive Otsu segmentation[76], allowing us to extract the objects that most likely belong to the given shape class.

Computational resources

All the FDK, MBIR, CAD-DLMBIR training and testing are done on an NVIDIA DGX with eight A100-SXM4-40GB GPUs with Ampere architecture.

DATA AVAILABILITY

The authors declare that the data supporting the findings of this study are available within the article and its supplementary information files or from the corresponding authors on reasonable request.

CODE AVAILABILITY

We implemented the MBIR algorithm using the pyMBIR package[77] freely available at https://github.com/svvenkatakrishnan/pyMBIR. The CAD-DLMBIR code is under DOE's copyright with DOE ID number: 90000193. Please contact the corresponding author for accessing the code.

Received: 29 June 2022; Accepted: 5 May 2023;
Published online: 30 May 2023

REFERENCES

1. Lu, Q. Y. & Wong, C. H. Additive manufacturing process monitoring and control by non-destructive testing techniques: challenges and in-process monitoring. *Virtual Phys. Prototyp.* **13**, 39–48 (2018).
2. Mandache, C. Overview of non-destructive evaluation techniques for metal-based additive manufacturing. *Mater. Sci. Technol.* **35**, 1007–1015 (2019).
3. Koester, L., Taheri, H., Bigelow, T. & Bond, L. Nondestructive testing for metal parts fabricated using powder based additive manufacturing. *Mater. Eval.* **76**, 514–524 (2018).
4. Su, Z. et al. Artificial neural network approach for multiphase segmentation of battery electrode nano-CT images. *NPJ Comput. Mater.* **8**, 1–11 (2022).
5. Lu, X. et al. 3D microstructure design of lithium-ion battery electrodes assisted by X-ray nano-computed tomography and modelling. *Nat. Commun.* **11**, 1–13 (2020).
6. Ziertmann, A., Jahnke, P., Kerscher, S., Koch, M. & Holub, W. Robot guided computed tomography—production monitoring in automotive industry 4.0. *J. Jpn. Soc. Precis. Eng.* **86**, 316–322 (2020).
7. Bauer, W., Bessler, F. T., Zabler, E. & Bergmann, R. B. Computer tomography for nondestructive testing in the automotive industry. In *Developments in X-ray Tomography IV*, vol. 5535, 464–472 (SPIE, 2004).
8. Galos, J. et al. Novel non-destructive technique for detecting the weld fusion zone using a filler wire of high X-ray contrast. *NDT E Int.* **124**, 102537 (2021).
9. Misokefalou, D., Papoutsidakis, P. & Priniotakis, P. Non-destructive testing for quality control in automotive industry. *Int. J. Eng. Appl. Sci. Technol.* **7**, 349–355 (2022).
10. Yusuke, K. et al. Investigation of industrial die-cast Al-alloys using X-ray micro-computed tomography and machine learning approach for CT segmentation. *Prod. Eng.* **17**, 291–305 (2023).
11. Wang, L., Limodin, N., El Bartali, A. & Charkaluk, E. Coupling of X-ray computed tomography and surface in situ analysis combined with digital image correlation method to study low cycle fatigue damage micromechanisms in lost foam casting A319 alloy. *Fatigue Fract. Eng. Mater. Struct.* **44**, 916–932 (2021).
12. Błachnio, J., Chalimoniuk, M., Kułaszka, A., Borowczyk, H. & Zasada, D. Exemplification of detecting gas turbine blade structure defects using the X-ray computed tomography method. *Aerospace* **8**, 119 (2021).
13. Shen, C. et al. Composition-induced microcrack defect formation in the twin-wire plasma arc additive manufacturing of binary tial alloy: An X-ray computed tomography-based investigation. *J. Mater. Res. Technol.* **36**, 4974–4985 (2021).
14. Kirka, M. et al. Analysis of data streams for qualification and certification of inconel 738lc airfoils processed through electron beam melting. In *Structural Integrity of Additive Manufactured Materials and Parts* (ASTM International, 2020).
15. Helmreich, G. W., Richardson, D., Venkatakrishnan, S. & Ziabari, A. Method for measurement of triso kernel and layer volumes by X-ray computed tomography. *J. Nucl. Mater.* **539**, 152255 (2020).
16. Li, Y., Parkinson, D. Y., Feng, J., Xia, C.-h & Gong, X. Quantitative X-ray tomographic analysis reveals calcium precipitation in cataractogenesis. *Sci. Rep.* **11**, 1–9 (2021).
17. Feldkamp, L. A., Davis, L. C. & Kress, J. W. Practical cone-beam algorithm. *Josa a* **1**, 612–619 (1984).
18. Bauza, M. B. et al. Realization of industry 4.0 with high speed CT in high volume production. *CIRP J. Manuf. Sci. Technol.* **22**, 121–125 (2018).
19. Zanini, F., Sorgato, M., Savio, E. & Carmignato, S. Dimensional verification of metal additively manufactured lattice structures by X-ray computed tomography: Use of a newly developed calibrated artefact to achieve metrological traceability. *Addit. Manuf.* **47**, 102229 (2021).
20. Lifton, J. & Liu, T. An adaptive thresholding algorithm for porosity measurement of additively manufactured metal test samples via X-ray computed tomography. *Addit. Manuf.* **39**, 101899 (2021).
21. Dahmen, T. et al. Characterization of channels made by laser powder bed fusion and binder jetting using X-ray CT and image analysis. *Addit. Manuf.* **36**, 101445 (2020).
22. Lu, Q., Nguyen, N., Hum, A., Tran, T. & Wong, C. Identification and evaluation of defects in selective laser melted 316l stainless steel parts via in-situ monitoring and micro computed tomography. *Addit. Manuf.* **35**, 101287 (2020).
23. Laleh, M. et al. A critical insight into lack-of-fusion pore structures in additively manufactured stainless steel. *Addit. Manuf.* **38**, 101762 (2021).
24. Gobert, C. et al. Porosity segmentation in X-ray computed tomography scans of metal additively manufactured specimens with machine learning. *Addit. Manuf.* **36**, 101460 (2020).
25. Klingaa, C., Dahmen, T., Baier, S., Mohanty, S. & Hattel, J. X-ray CT and image analysis methodology for local roughness characterization in cooling channels made by metal additive manufacturing. *Addit. Manuf.* **32**, 101032 (2020).
26. Vayssette, B., Saintier, N., Brugger, C., El May, M. & Pessard, E. Numerical modelling of surface roughness effect on the fatigue behavior of ti-6al-4v obtained by additive manufacturing. *Int J. Fatigue* **123**, 180–195 (2019).
27. Gockel, J., Sheridan, L., Koerper, B. & Whip, B. The influence of additive manufacturing processing parameters on surface roughness and fatigue life. *Int. J. Fatigue* **124**, 380–388 (2019).
28. Naresh, K., Khan, K., Umer, R. & Cantwell, W. J. The use of X-ray computed tomography for design and process modeling of aerospace composites: A review. *Mater. Des.* **190**, 108553 (2020).
29. Yan, W. et al. Data-driven multi-scale multi-physics models to derive process–structure–property relationships for additive manufacturing. *Computational Mech.* **61**, 521–541 (2018).
30. Rupal, B. S., Anwer, N., Secanell, M. & Qureshi, A. J. Geometric tolerance and manufacturing assemblability estimation of metal additive manufacturing (am) processes. *Mater. Des.* **194**, 108842 (2020).
31. Zanini, F., Carmignato, S. & Savio, E. Assembly analysis of titanium dental implants using X-ray computed tomography. *Proc. euspen.* 489–490 (2017).
32. Khosravani, M. R. & Reinicke, T. On the use of X-ray computed tomography in assessment of 3D-printed components. *J. Nondestr. Eval.* **39**, 1–17 (2020).
33. Vásárhelyi, L., Kónya, Z., Kukovecz, Á. & Vajtai, R. Microcomputed tomography–based characterization of advanced materials: A review. *Mater. Today Adv.* **8**, 100084 (2020).
34. Carmignato, S., Dewulf, W. & Leach, R. *Industrial X-ray computed tomography*, vol. 10 (Springer International Publishing, 2018).
35. Ziabari, A. et al. Beam Hardening Artifact Reduction in X-ray CT Reconstruction of 3D Printed Metal Parts Leveraging Deep Learning and CAD Models. In *Proceedings of the ASME 2020 International Mechanical Engineering Congress and Exposition (IMECE)*, vol. 84492, V02BT02A043 (American Society of Mechanical Engineers, 2020). https://www.euspen.eu/knowledge-base/ICE17276.pdf.
36. Jin, P., Bouman, C. A. & Sauer, K. D. A model-based image reconstruction algorithm with simultaneous beam hardening correction for X-ray CT. *IEEE Trans. Comput. Imaging* **1**, 200–216 (2015).
37. Abella, M., Martínez, C., Desco, M., Vaquero, J. J. & Fessler, J. A. Simplified statistical image reconstruction for X-ray CT with beam-hardening artifact compensation. *IEEE Trans. Med. Imaging* **39**, 111–118 (2019).
38. Ruth, V., Kolditz, D., Steiding, C. & Kalender, W. A. Metal artifact reduction in X-ray computed tomography using computer-aided design data of implants as prior information. *Invest. Radiol.* **52**, 349–359 (2017).
39. Ha, S. & Mueller, K. Metal artifact reduction in X-ray CT via ray profile correction. *Appl. Sci.* **10**, 66 (2019).
40. Tan, Y. et al. Simulation-aided investigation of beam hardening induced errors in CT dimensional metrology. *Meas. Sci. Technol.* **25**, 064014 (2014).
41. Van de Casteele, E., Van Dyck, D., Sijbers, J. & Raman, E. An energy-based beam hardening model in tomography. *Phys. Med. Biol.* **47**, 4181 (2002).
42. Hammersberg, P. & Mångård, M. Correction for beam hardening artefacts in computerised tomography. *J. Xray. Sci. Technol.* **8**, 75–93 (1998).
43. Ghani, M. U. & Karl, W. C. Fast enhanced ct metal artifact reduction using data domain deep learning. *IEEE Trans. Computational Imaging* **6**, 181–193 (2019).
44. Park, H. S., Lee, S. M., Kim, H. P., Seo, J. K. & Chung, Y. E. CT sinogram-consistency learning for metal-induced beam hardening correction. *Med. Phys.* **45**, 5376–5384 (2018).
45. Martin, L., Tuysuzoglu, A., Ishwar, P. & Karl, W. C. Joint metal artifact reduction and material discrimination in X-ray CT using a learning-based graph-cut method. In *Computational Imaging XII*, vol. 9020, 48–57 (SPIE, 2014).
46. Xu, S. & Dang, H. Deep residual learning enabled metal artifact reduction in CT. In *Medical Imaging 2018: Physics of Medical Imaging*, vol. 10573, 950–955 (SPIE, 2018).
47. Kalare, K., Bajpai, M., Sarkar, S. & Munshi, P. Deep neural network for beam hardening artifacts removal in image reconstruction. *Appl. Intell.* **52**, 6037–6056 (2022).
48. Ketcham, R. A. & Hanna, R. D. Beam hardening correction for X-ray computed tomography of heterogeneous natural materials. *Comput. Geosci.* **67**, 49–61 (2014).
49. Ziabari, A. et al. Model Based Iterative Reconstruction With Spatially Adaptive Sinogram Weights for Wide-cone Cardiac CT. In *Proc. 5th Intl. Mtg. on Image Formation in X-ray CT*, 15–19 (Salt Lake City, Utah, 2018).
50. Ronneberger, O., Fischer, P. & Brox, T. U-net: Convolutional networks for biomedical image segmentation. In *International Conference on Medical image computing and computer-assisted intervention*, 234–241 (Springer, 2015).
51. Bouman, C. A. *Foundations of Computational Imaging: A Model-Based Approach* (SIAM, 2022).
52. Yu, Z., Thibault, J.-B., Bouman, C. A., Sauer, K. D. & Hsieh, J. Fast model-based X-ray CT reconstruction using spatially nonhomogeneous icd optimization. *IEEE Trans. Img. Process.* **20**, 161–175 (2010).
53. Kak, A. C. & Slaney, M. *Principles of computerized tomographic imaging* (SIAM, 2001).

54. Tang, J., Nett, B. E. & Chen, G.-H. Performance comparison between total variation (tv)-based compressed sensing and statistical iterative reconstruction algorithms. *Phys. Med. Biol.* **54**, 5781 (2009).
55. Tian, Z., Jia, X., Yuan, K., Pan, T. & Jiang, S. B. Low-dose CT reconstruction via edge-preserving total variation regularization. *Phys. Med. Biol.* **56**, 5949 (2011).
56. Liu, Y., Ma, J., Fan, Y. & Liang, Z. Adaptive-weighted total variation minimization for sparse data toward low-dose X-ray computed tomography image reconstruction. *Phys. Med. Biol.* **57**, 7923 (2012).
57. Balke, T. et al. Separable models for cone-beam mbir reconstruction. *Electron. Imaging* **2018**, 181–181 (2018).
58. Venkatakrishnan, S., Mohan, K. A., Ziabari, A. K. & Bouman, C. A. Algorithm-driven advances for scientific CT instruments: From model-based to deep learning-based approaches. *IEEE Signal Process. Mag*. (2022).
59. Thibault, J.-B., Sauer, K. D., Bouman, C. A. & Hsieh, J. A three-dimensional statistical approach to improved image quality for multislice helical ct. *Med. Phys.* **34**, 4526–4544 (2007).
60. Slotwinski, J. A., Garboczi, E. J. & Hebenstreit, K. M. Porosity measurements and analysis for metal additive manufacturing process control. *J. Res. Natl Inst. Stand. Technol.* **119**, 494 (2014).
61. Chen, Z., Han, C., Gao, M., Kandukuri, S. Y. & Zhou, K. A review on qualification and certification for metal additive manufacturing. *Virtual Phys. Prototyp.* **17**, 382–405 (2022).
62. Bahl, S. et al. Al-Cu-Ce(-Zr) alloys with an exceptional combination of additive processability and mechanical properties. *Addit. Manuf.* **48**, 102404 (2021).
63. Bahl, S. et al. Elevated Temperature Ductility Dip in an Additively Manufactured Al-Cu-Ce Alloy. *Acta Mater.* **220**, 117285 (2021).
64. Venkatakrishnan, S. V. pyMBIR. https://github.com/svvenkatakrishnan/pyMBIR. Accessed: 2021–2022.
65. Tigre. https://github.com/CERN/TIGRE. Accessed: 2021–2022.
66. Bouman, C. Openmbir-ConeBeam. https://github.com/cabouman/mbircone. Accessed: 2021–2022.
67. Otsu, N. A threshold selection method from gray-level histograms. *IEEE Trans. Syst. Man Cybern.* **9**, 62–66 (1979).
68. Ziabari, A. et al. 2.5D deep learning for CT image reconstruction using a multi-gpu implementation. In *2018 52nd Asilomar Conference on Signals, Systems, and Computers*, 2044-2049 (IEEE, 2018).
69. Goodfellow, I., Bengio, Y. & Courville, A. *Deep Learning* (MIT Press, 2016). http://www.deeplearningbook.org.
70. Kingma, D. P. & Ba, J. Adam: A method for stochastic optimization. In *International Conference on Learning Representations (ICLR)*, vol. 9 (2015).
71. Parker, D. L. Optimal short scan convolution reconstruction for fan beam CT. *Med. Phys.* **9**, 254–257 (1982).
72. Storn, R. & Price, K. Differential evolution–a simple and efficient heuristic for global optimization over continuous spaces. *J. Glob. Optim.* **11**, 341–359 (1997).
73. Sundar, V. et al. Flaw identification in additively manufactured parts using X-ray computed tomography and destructive serial sectioning. *J. Mater. Eng. Perform.* **30**, 4958–4964 (2021).
74. Snow, Z., Scime, L., Ziabari, A., Fisher, B. & Paquit, V. Observation of spatter-induced stochastic lack-of-fusion in laser powder bed fusion using in situ process monitoring. *Addit. Manuf.* **61**, 103298 (2023).
75. Sato, Y. et al. Tissue classification based on 3d local intensity structures for volume rendering. *IEEE Trans. Vis. Comput. Graph.* **6**, 160–180 (2000).
76. Huang, D.-Y. & Wang, C.-H. Optimal multi-level thresholding using a two-stage otsu optimization approach. *Pattern Recognit. Lett.* **30**, 275–284 (2009).
77. Venkatakrishnan, S. V. pyMBIR. Tech. Rep., Oak Ridge National Lab.(ORNL), Oak Ridge, TN (United States) (2019).

ACKNOWLEDGEMENTS

This manuscript has been authored by UT-Battelle, LLC, under contract DE-AC05-00OR22725 with the US Department of Energy (DOE).Research sponsored by the US Department of Energy, Office of Energy Efficiency and Renewable Energy, Advanced Manufacturing Office and Technology Commercialisation Fund (TCF-21-24881), under contract DE-AC05-00OR22725 with UT-Battelle, LLC. The US government retains and the publisher, by accepting the article for publication, acknowledges that the US government retains a nonexclusive, paid-up, irrevocable, worldwide license to publish or reproduce the published form of this manuscript, or allow others to do so, for US government purposes. DOE will provide public access to these results of federally sponsored research in accordance with the DOE Public Access Plan (http://energy.gov/downloads/doe-public-access-plan).

AUTHOR CONTRIBUTIONS

A.Z. performed design of experiments (DOE), developed the CAD-DLMBIR algorithm, analyzed the data, and wrote the manuscript. S.V.V. contributed to DOE, development of ideas, algorithms, and writing and analysis in the manuscript. Z.S. contributed to writing and analysis through registration to optical microscopy and PoD analysis. S.G. performed the part preparation and pycnometery and helped with writing. P.Bi. helped with writing and developing ideas. P.Br. performed the experiment and helped with analysis. C.F. performed the experiment and helped with analysis. P.Bh. designed the CAD geometry and helped with analysis. A.L. and M. S. helped with analysis and segmentation. A.P. and R.D. contributed to DOE, printing parameters, initial design, and writing the manuscript. A.Z., R.D., A.P., and V.P. supported/funded different parts of this project.

COMPETING INTERESTS

The authors declare no competing interests.

ADDITIONAL INFORMATION

Supplementary information The online version contains supplementary material available at https://doi.org/10.1038/s41524-023-01032-5.

Correspondence and requests for materials should be addressed to Amirkoushyar Ziabari.

Reprints and permission information is available at http://www.nature.com/reprints

Publisher's note Springer Nature remains neutral with regard to jurisdictional claims in published maps and institutional affiliations.